

Simulation model of Reactive Nitrogen species in an urban atmosphere using a Deep neural network: RNDv1.0

Junsu Gil¹, Meehye Lee¹, Jeonghwan Kim², Gangwoong Lee², Joonyoung Ahn³, Cheol-Hee Kim⁴

¹ Department of Earth and Environmental Sciences, Korea University, Seoul, South Korea

² Department of Environmental Science, Hankuk University of Foreign Studies, Yongin, South Korea

³ Air Quality Forecasting Center, Climate and Air Quality Research Department, National Institute of Environmental Research (NIER), Incheon, South Korea

⁴ Department of Atmospheric Sciences, Pusan National University, Busan, South Korea

Correspondence to: Meehye Lee (meehye@korea.ac.kr)

Abstract. Nitrous acid (HONO) plays an important role in the formation of ozone and fine aerosols in the urban atmosphere. In this study, a new simulation approach is presented to calculate the HONO mixing ratios using a deep neural technique based on measured variables. The “Reactive Nitrogen species simulation using deep neural network (RND)” is implemented in Python. The first version of RND (RNDv1.0) is trained, validated, and tested with HONO measurement data obtained in Seoul from 2016 to 2021. RNDv1.0 is constructed using k-fold cross validation and evaluated with index of agreement, correlation coefficient, root mean squared error, and mean absolute error. The results show that RNDv1.0 adequately represents the main characteristics of the measured HONO, and it is thus proposed as a supplementary model for calculating the HONO mixing ratio in a polluted urban environment.

1. Introduction

Surface ozone (O_3) pollution has worsened over continental areas (Arnell et al., 2019; Monks et al., 2015; Varotsos et al., 2013; IPCC, 2014). Particularly, a warmer climate is expected to increase the surface O_3 concentrations and peak levels in polluted regions depending on its precursor levels (IPCC, 2021). As a short-lived climate pollutant (SLCP), O_3 interacts with the global temperature via positive feedback (Shindell et al., 2013; Myhre et al., 2017; Stevenson et al., 2013). Therefore, accurate predictions of the mixing ratios and variations of the surface O_3 are essential. While operational models such as the community multiscale air

34 quality (CMAQ) have been widely used for this purpose, uncertainties still arise from poorly
35 understood chemical mechanisms involving reactive nitrogen oxides (NO_y) and volatile organic
36 compounds (VOCs), and the lack of their measurements (Mallet and Sportisse, 2006;Canty et
37 al., 2015;Akimoto et al., 2019;Shareef et al., 2019;Cheng et al., 2022).

38 In the urban atmosphere, NO_y typically includes NO_x ($\text{NO} + \text{NO}_2$), HONO, HNO_3 ,
39 organic nitrates (e.g., PAN), NO_3 , N_2O_3 , and particulate NO_3^- . These species are produced and
40 recycled through photochemical reactions until they are removed through wet or dry deposition
41 (Liebmann et al., 2018;Brown et al., 2017;Wang et al., 2020;Li et al., 2020). NO_y plays an
42 important role in critical environmental issues concerning the Earth's atmosphere from local air
43 pollution to global climate change (Sun et al., 2011;Ge et al., 2019). The oxidation of NO to
44 NO_2 and finally to HNO_3 is the backbone of the chemical mechanism producing ozone (O_3)
45 and $\text{PM}_{2.5}$ (particulate matter with size $\leq 2.5 \mu\text{m}$), and determines the oxidization capacity of
46 the atmosphere. Recently, as O_3 has still increased even with decreasing NO_x emissions over
47 many regions, including East Asia, interest in the heterogeneous reaction of NO_y , which is yet
48 to be understood, has increased (Brown et al., 2017;Stadtler et al., 2018). Currently, the lack of
49 measurement of individual NO_y species is hindering a comprehensive understanding of the
50 heterogeneous reactions (Anderson et al., 2014;Wang et al., 2017b;Chen et al., 2018b;Akimoto
51 and Tanimoto, 2021;Stadtler et al., 2018).

52 In particular, the evidence for the heterogeneous formation of HONO in relation to high
53 $\text{PM}_{2.5}$ and O_3 occurrences in urban areas is increasing (e.g., (Li et al., 2021b)). As an OH
54 reservoir, HONO expedites the photochemical reactions involving VOCs and NO_x in the early
55 morning, leading to O_3 and fine aerosol formation. Nonetheless, its formation mechanism has
56 not been elucidated sufficiently enough to be constrained in conventional photochemical
57 models. In addition to the reaction of NO with OH (Bloss et al., 2021), various pathways of
58 HONO formation have been suggested via laboratory experiments, field measurements, and
59 model simulations: direct emissions from vehicles (Li et al., 2021a) and soil (Bao et al., 2022),
60 photolysis of particulate nitrate (Gen et al., 2022), and heterogeneous conversion of NO_2 on
61 various aerosol surfaces (Jia et al., 2020), ground surface (Meng et al., 2022), and microlayers
62 of the sea surface (Gu et al., 2022). Among these, the heterogeneous reaction mechanism on the
63 surface is of major interest.

64 HONO has been mostly measured during intensive campaigns in urban areas using
65 various techniques, such as a long path absorption photometer (Kleffmann et al., 2006;Xue et
66 al., 2019), chemical ionization mass spectrometry (Levy et al., 2014;Roberts et al., 2010), ion
67 chromatography (VandenBoer et al., 2014;Gil et al., 2020;Ye et al., 2016;Xu et al., 2019),
68 monitor for aerosols and gases in ambient air (MARGA) (Xu et al., 2019), and quantum cascade
69 - tunable infrared laser differential absorption spectrometry (QC-TILDAS) (Lee et al., 2011;Gil
70 et al., 2021). Among these methods, QC-TILDAS has served as a reference for the
71 intercomparison of measurement data obtained using different techniques due to its high time
72 resolution and stability (Pinto et al., 2014). Previous studies have reported that the maximum
73 HONO of several ppb levels has been observed at nighttime. In comparison, the WRF-Chem
74 and RACM2 model captured approximately 67 %–90 % of the observed HONO in megacities
75 such as Beijing (Tie et al., 2013;Liu et al., 2019).

76 In recent years, machine learning (ML) methods have been employed in the
77 atmospheric science field for pattern classification (e.g., new particle formation event) and
78 forecasting and spatiotemporal modeling of O₃ and PM_{2.5} (Arcomano et al., 2021;Shahriar et
79 al., 2020;Krishnamurthy et al., 2021;Cui and Wang, 2021;Joutsensaari et al., 2018;Chen et al.,
80 2018a;Kang et al., 2021). Among the ML methods, the neural network (NN) architecture is
81 widely used owing to its powerful ability to process large volumes of data. In particular, a
82 multilayer artificial NN (ANN), referred to as a deep NN (DNN), employs statistical methods
83 to learn nonlinear relationships within the data and yield optimal solutions for a target species
84 without prior knowledge of the underlying physicochemical processes (Reichstein et al.,
85 2019;Schultz et al., 2021). DNN is more beneficial than other NN architecture, such as
86 convolution NN or long-short term memory, because it works well for discrete spatiotemporal
87 data. Generally, the performance of DNN is similar to or better than that of other ML methods
88 for small as well as large datasets (Baek and Jung, 2021;Dang et al., 2021;Sumathi and
89 Pugalendhi, 2021).

90 The DNN method requires lots of data to employ it as atmospheric chemical constituent
91 estimation; therefore, the size of the measurement data is a limiting factor for trace species,
92 such as HONO, that are not routinely measured. In this regard, previous studies had been
93 attempted to estimate the daily average HONO mixing ratio by employing ensemble ML models
94 with satellite measurements (Cui and Wang, 2021). Furthermore, a simple NN architecture

95 using ground measurement variables that is believed to be deeply involved in HONO formation,
96 was used to calculate the hourly HONO mixing ratio (Gil et al., 2021). The accuracy of the
97 hourly HONO estimated from input variables, such as aerosol surface areas and mixed layer
98 height, is rated better than the daily HONO estimate.

99 This study aims to develop a user-friendly “reactive nitrogen species simulation using
100 DNN’ model (RNDv1.0) that estimates the HONO mixing ratios from the real-time
101 measurements of criteria pollutants and meteorological variables. This study is the first to
102 calculate the HONO mixing ratios using RNDv1.0. The entire construction process is
103 comprehensively described, and the performance is evaluated via comparison with the results
104 of simulations using a commonly used model and observations over several years.

105

106 **2. Model description**

107

108 The RNDv1.0 development follows systematic steps that are similar to a general ML
109 model construction workflow, including data collection, preprocessing data, building the DNN,
110 training, and validating the model, and testing the model performance (Figure 1). RNDv1.0 is
111 written in Python, and the libraries necessary to build and operate RNDv1.0 are listed in Table
112 1. The dataset used to train, test, and validate can be downloaded from Gil (2021).

113

114 **2.1. Collection of measurement data for model construction**

115

116 To construct RNDv1.0, measurement data were obtained, including HONO, reactive
117 gases, and meteorological variables. Note that the HONO measurement data were used for
118 model construction but not required to run the RND model. The HONO mixing ratio was
119 measured in Seoul using a QC-TILDAS system during May–June 2016, June 2018, and April–
120 June 2019 (Lee et al., 2011; Gil et al., 2021), and a MARGA system during May–June 2021 and
121 October–November 2021 (Gil, 2022). When testing and evaluating the atmospheric HONO
122 measurement methods, QC-TILDAS was chosen as the reference method to compare the
123 ambient HONO mixing ratios measured using several different techniques owing to its

124 advantages of low detection limits (~0.1 ppbv) and high temporal resolution (Pinto et al., 2014).
125 More details on measurements can be found elsewhere (Gil et al., 2021;Gil, 2022).

126 HONO was measured at the Olympic Park (37.52° N, 127.12° E) during the Korea–
127 United States Air Quality (KORUS-AQ) study in 2016 (Kim et al., 2020;Gil et al., 2021), at the
128 campus of Korea University (37.59° N, 127.03° E) in 2018 and 2021, and at the site near the
129 Korea University campus (37.59° N, 127.08° E) in 2019 (NIER, 2020) (Figure S1). In addition
130 to HONO, trace gases including O₃, NO₂, CO, and SO₂ as well as meteorological variables
131 including temperature (T), relative humidity (RH), wind speed (WS), and wind direction (WD)
132 were measured. Note that HONO was not significantly correlated with any of these variables
133 (Figure S2). The measurement statistics for the entire experimental periods are presented in
134 Table 2 and Table S1. In brief, the 10th and 90th percentile mixing ratios of hourly HONO, NO₂,
135 and O₃, were 0.3 and 2.0 ppbv, 10.0 and 47.0 ppbv, and 8.0 and 75.0 ppbv, respectively.

136

137 **2.2. Data preprocessing**

138

139 The observation dataset was prepared for RNDv1.0 model construction. As input
140 variables, hourly measurements of chemical and meteorological variables were used, including
141 the mixing ratios of O₃, NO₂, CO, and SO₂, along with T, RH, WS, WD, and solar zenith angle
142 (SZA) to estimate the target species, HONO, as the output. The WD in degrees was converted
143 to a cosine value for continuity. In the last step of data processing, hourly measurement sets
144 were removed from the input data set if any of the nine variables were missing. Finally, 54.2 %
145 of all the available measurement data (2847 data points) were used to construct and evaluate
146 RNDv1.0.

147 Since the measurements of the considered nine variables varied over a wide range in
148 different units, they were normalized to avoid bias during the calculations. Among the widely
149 used normalization methods, *min–max scaling* method was adopted, and the input variables
150 were normalized against the minimum and maximum values herein (Eq. 1):

151

$$152 \quad x_{\text{sca}} = \frac{x_{\text{raw}} - F_2(X)}{F_1(X)}, \quad (\text{Eq. 1})$$

153

154 where x_{raw} is the raw data, x_{sca} is the scaled value, and the scale factors of F_1 and F_2 correspond
155 to the maximum-minimum and minimum values of the input variable (X), respectively, which
156 are listed in Table 2.

157

158 **2.3. Neural network architecture and hyperparameters**

159

160 The network was built using the above input variables to calculate HONO. RNDv1.0
161 comprises five hidden layers (Figure 2), which employ an exponential linear unit (ELU) as an
162 activation function (Eq. 2).

163

$$164 \quad \text{ELU: } \phi(x) = \begin{cases} e^x - 1 & (x < 0) \\ x & (x \geq 0) \end{cases}. \quad (\text{Eq. 2})$$

165

166 In a DNN, an activation function creates a nonlinear relationship between an input
167 variable and an output variable. When constructing a DNN model, ELU affords the advantage
168 of a fast training process and exhibits better performance in handling negative values than other
169 activation functions (Wang et al., 2017a; Ding et al., 2018). Moreover, the mean squared error
170 and Adam optimizer were applied as the loss function and optimization function, respectively.
171 The learning rate, epoch, and batch were set as 0.01, 100, and 32, respectively.

172

173 **2.4. Model training and k-fold cross validation**

174

175 RNDv1.0 was trained, validated, and tested with the HONO measurements obtained
176 during May–June 2016 and June 2018, April–June 2019, and May–June 2021 and October–
177 November 2021, respectively (Figure 3). The number of data used for the training and
178 validation was 1122 and that for testing was 1725.

179 Using the hyperparameters specified in the previous section, the model performance
 180 was first validated using the k-fold cross validation (KFCV) method, which is especially useful
 181 for small datasets (Bengio and Grandvalet, 2003). In the KFCV method (Figure 3), the entire
 182 data are randomly divided into k subsets, of which k – 1 sets are used for training and the
 183 remaining one is used for validation. In this study, k was set to 5. The accuracy was determined
 184 via index of agreement (IOA), which is expressed as follows (Eq. 3):

$$186 \quad IOA = 1 - \frac{\sum_{i=1}^n (O_i - P_i)^2}{\sum_{i=1}^n (|P_i - \bar{O}| + |O_i - \bar{O}|)^2}, \quad (Eq. 3)$$

187 where O_i , P_i , \bar{O} , and n are the observed value, predicted value, average of the observed values,
 188 and number of nodes, respectively.

190 As IOA varies according to the number of nodes, it was calculated for the measured
 191 ($HONO_{obs}$) and calculated ($HONO_{mod}$) mixing ratios by varying the number of nodes from 0 to
 192 100 in each hidden layer. The best performance was obtained with 41 nodes, for which the
 193 average IOA was 0.89 ± 0.01 (Figure 4). The high IOA value signifies that the performance of
 194 RNDv1.0 is adequate, and it is capable of simulating the ambient HONO mixing ratio using the
 195 routinely measured criteria pollutants and meteorological variables.

196 The performance of RNDv1.0 was compared with that of other models, including
 197 CMAQv5.3.1 (Appel et al., 2021), random forest (RF), and single-layer ANN (Gil et al., 2021),
 198 using the 2016 measurement data. The RF model was constructed using the KFCV method and
 199 the same input variables as RNDv1.0 (Figure S4). Its performance was evaluated based on mean
 200 absolute error (MAE), root mean square deviation (RMSE), and Pearson correlation coefficient
 201 (r):

$$203 \quad MAE = \frac{\sum_{i=1}^n |O_i - P_i|}{n}, \quad (Eq. 4)$$

$$204 \quad RMSE = \sqrt{\frac{\sum_{i=1}^n (O_i - P_i)^2}{n}}, \quad (Eq. 5)$$

$$205 \quad r = \frac{cov(O,P)}{\sigma_O \sigma_P}, \quad (Eq. 6)$$

206

207 where σ and *cov* denote the standard deviation and covariance, respectively.

208 All models except CMAQ simulated the measured HONO mixing ratio fairly well
209 (Figure 5). CMAQ not only underestimated the measured HONO but also failed to represent its
210 diurnal variation (Figure 6). The statistical information about the performance of the four
211 models is presented in Table 3. The mean HONO mixing ratio measured and calculated using
212 CMAQ, RF, ANN, and RNDv1.0 was 0.94, 0.09, 0.95, 0.88, and 0.89 ppbv, respectively. Of the
213 four models, RF exhibited the best performance followed by RND. ANN advantageously
214 calculates HONO more accurately than RND as it uses more input variables, but it has a lower
215 data capture rate (41.5 %) compared to RND (97.7 %) or RF (85.3 %).

216

217 **2.5. Model test**

218

219 RNDv1.0 and the RF model were tested using data obtained in June 2018, April 2019,
220 and May–June 2021 and October–November in 2021, which were not used for RNDv1.0
221 training (Figure 3). Note that the RF model outperformed the other three models in the training
222 and validation process (Figure 5). Although the performance of RNDv1.0 was slightly lower
223 than that of the RF model, simulated and measured HONO mixing ratios were in good
224 agreement. Interestingly, the performance of the RF model was much worse than RNDv1.0 in
225 the testing process (Figure 7). The IOA and correlation coefficient of the RF model were
226 extremely low (0.29 and -0.02 , respectively).

227 The performance of RNDv1.0 was slightly lower than that of the RF model, but it well
228 traced the HONO mixing ratio. Among the test dataset, the early winter (October–November)
229 data are particularly valuable for demonstrating the applicability of RNDv1.0 because they stem
230 from different weather conditions than the training dataset. For example, HONO mixing ratios
231 reached over 4 ppbv when the daily average PM_{2.5} concentration increased to 120 $\mu\text{g m}^{-3}$ during
232 severe haze pollution events. Therefore, in the next step, the performance of RNDv1.0 was
233 compared for the two cases by dividing the testing dataset into a group in which all input
234 variables fall within the range of the training dataset and a group which does not meet this

235 criterion. In RNDv1.0, there was no significant difference in performance between the two
236 groups (Figure S5 and Table S2). When the data in which at least one input variable does not
237 fall within the range of the training dataset were excluded from the test dataset, no significant
238 difference was observed in the performance of RNDv1.0 between the two that meet same
239 atmospheric conditions or do not meet the criteria (Figure S5 and Table S2). These extreme
240 atmospheric conditions can make the model performance be worsened. Except for these
241 extremes, RNDv1.0 well traced the variation of the HONO mixing ratio. These results
242 demonstrate the applicability of RNDv1.0, which is not strictly constrained by atmospheric
243 conditions. The influence of input variable are further analyzed in the next section.

244

245 **2.6. Bootstrap test and feature importance**

246

247 A simple bootstrapping test was conducted for both RNDv1.0 and the RF model to
248 evaluate the relative importance of the input variable to the HONO estimates. In this analysis,
249 each variable was set to zero and MAE was calculated as an evaluation metrics (Kleinert et al.,
250 2021). Among the nine input variables of RNDv1.0, NO₂ was found to have the greatest
251 influence on HONO concentration, followed by RH and T (Table 5). The highest MAE of 0.59
252 ppbv could be considered as the maximum uncertainty of RNDv1.0 due to the input variable.
253 The bootstrap test result well agreed with that of our previous study (Gil et al., 2021), where
254 more variables such as aerosol surface area and mixing layer height were incorporated into the
255 model, it highlights the crucial role of precursor gases and heterogeneous conversion in HONO
256 formation.

257 In contrast, in the RF model, O₃ was the most important variable. This is likely due to the
258 distinct inverse relationship between O₃ and HONO in the diurnal patterns, and the O₃
259 variations over a wide range. In conjunction with the evaluation of the test dataset presented in
260 the previous section, the results of the feature importance for the two models demonstrate the
261 ability of RNDv1.0 to simulate the HONO mixing ratio more adequately in urban areas
262 compared to the RF model. Thus, it is reasonable to state that RNDv1.0 constructed using
263 routinely measured criteria pollutants and meteorological variables can sufficiently capture the
264 HONO variability in the urban atmosphere.

265

266 **3. Operation and application of RNDv1.0**

267

268 The RNDv1.0 package is provided as an operational model, and the .h5 files that can
269 be opened in Python. To run RNDv1.0, the measurement data for nine input variables are
270 required and needed to be properly prepared, as described in Section 2.2. Once the input data
271 are ready, open RNDv1.0 with the input data files using the code provided in the example
272 (Figure S3). Then, RNDv1.0 calculates and presents the HONO results as scaled values (x_{sca}),
273 which then can be converted to the HONO mixing ratio (ppbv) via the two scale factors shown
274 in Table 2 (Eq. 5):

275

$$276 \quad \text{HONO (ppbv)} = \text{HONO}_{sca} \times F_1(\text{HONO}) + F_2(\text{HONO}). \quad (5)$$

277

278 The HONO calculated using Eq. 5 can be applied to an urban photochemical cycle
279 simulation. As is already known, the photolysis of HONO is a major source of OH radicals in
280 the early morning when the OH level is low, and this OH affects daytime O₃ formation through
281 photochemical reactions with VOCs and NO_x, which are primarily emitted during the morning
282 rush hour in urban areas. Furthermore, the OH produced from HONO promotes the
283 photochemical oxidation of SO₂ and VOCs, leading to aerosol formation. However, the HONO
284 formation mechanism is still poorly understood, which hinders the accurate simulation of O₃
285 and fine aerosols as well as HONO in conventional photochemical models.

286 The framework for 0-dimension atmospheric modeling (F0AM), which utilizes the
287 MCM v3.3.1 chemical reaction mechanisms (Wolfe et al., 2016), can be used to simulate the
288 diurnal variation of O₃ with the measurements of several reactive gases (NO, NO₂, CO, HCHO,
289 VOCs, and HONO). Detailed information about F0AM can be found in
290 (<https://sites.google.com/site/wolfegm/models>) and in previous studies (Wolfe et al., 2016; Gil
291 et al., 2020). When the F0AM model is run without HONO, it is unable to reproduce the
292 concentration and diurnal cycle of the observed O₃ (Figure 8). In comparison, the model well
293 simulates the O₃ within 2 ppbv when HONO is considered, which is the result of RND v1.0.

294 This is mainly due to the missing OH produced by HONO photolysis in the early morning. Its
295 production rate is estimated to be 0.57 pptv s^{-1} , contributing approximately 2.28 pptv to the OH
296 budget during 06:00–11:00 (Local Sun Time) (Gil et al., 2021). Given that OH is mainly
297 produced from the photolysis of O_3 under high sun, the early morning supply of OH from
298 HONO photolysis will expedite the photochemical cycle involving NO_x and VOCs, promoting
299 O_3 and secondary aerosol formation. The presence of HONO in the photochemical model
300 allows for the accurate estimation of OH radicals; thus, the incorporation of RNDv1.0 into
301 conventional models will improve their overall performance.

302

303 **4. Summary and implications**

304

305 In this study, we developed the RND model to calculate the mixing ratio of NO_y in
306 urban atmosphere using a DNN along with measurement data. The target species of RNDv1.0
307 is HONO, and its mixing ratio is calculated using criteria pollutants, including O_3 , NO_2 , CO,
308 and SO_2 , as well as meteorological variables, including T, RH, WS, WD, and SZA. These
309 variables are routinely measured through monitoring networks. RNDv1.0 was trained and
310 validated using the HONO measurements data obtained in Seoul by adopting a KFCV method
311 and tested with other HONO datasets. The test results demonstrate that RNDv1.0 adequately
312 captures the characteristic variation of HONO.

313 RNDv1.0 was constructed using the measurements made in a high NO_x environment where
314 the maximum NO_2 reached about 80 ppbv. During the measurement period, the HONO mixing
315 ratio was increased up to about 7 ppb under the influence of air masses originating from China.
316 When applying RNDv1.0 to regions or times heavily affected by transport, the model could
317 possibly underestimate the HONO level without more detailed information, such as
318 nanoparticles. Indeed, a previous study showed that HONO formation is closely related to the
319 surface area of particles with diameters in the range of hundreds of nanometers (Gil et al., 2021).
320 Nevertheless, RNDv1.0 is advantageously a relatively inexpensive test for measurement quality
321 control and location selection, and it supports the data used for traditional chemistry models
322 based on the current knowledge of the urban photochemical cycle. Therefore, RNDv1.0 can
323 serve as a supplementary tool for conventional forecasting models. Attempts are currently being

324 made to estimate ground HONO from satellite observations (Clarisse et al., 2011;Theys et al.,
325 2020;Armante et al., 2021), and RNDv1.0 will be useful for validating the satellite-derived
326 HONO.

327

328 **5. Acknowledgements**

329

330 This study was supported by the National Research Foundation of Republic of Korea
331 (2020R1A2C3014592) and Korea Institute of Science and Technology (KIST2E31650-22-
332 P019).

333

334 **6. Code availability**

335

336 The RND model codes (.h5 files) with preprocessed sample data can be downloaded from
337 (Gil, 2021).

338

339 **7. Author contributions**

340

341 JG and ML designed the manuscript and developed the model code. JK, GL, and JA
342 provided the HONO measurements and CK provided the CMAQ model data. All the authors
343 contributed to the manuscript.

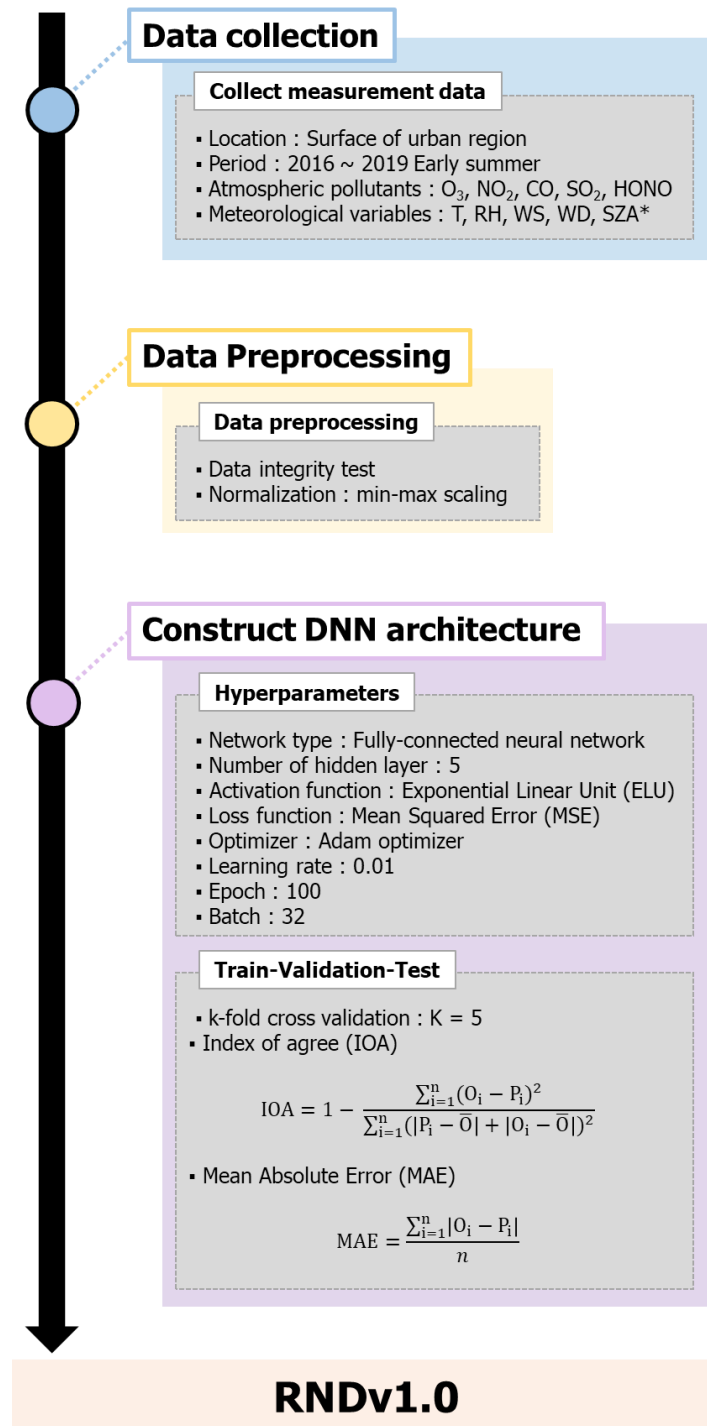
344

345 **8. Competing interests**

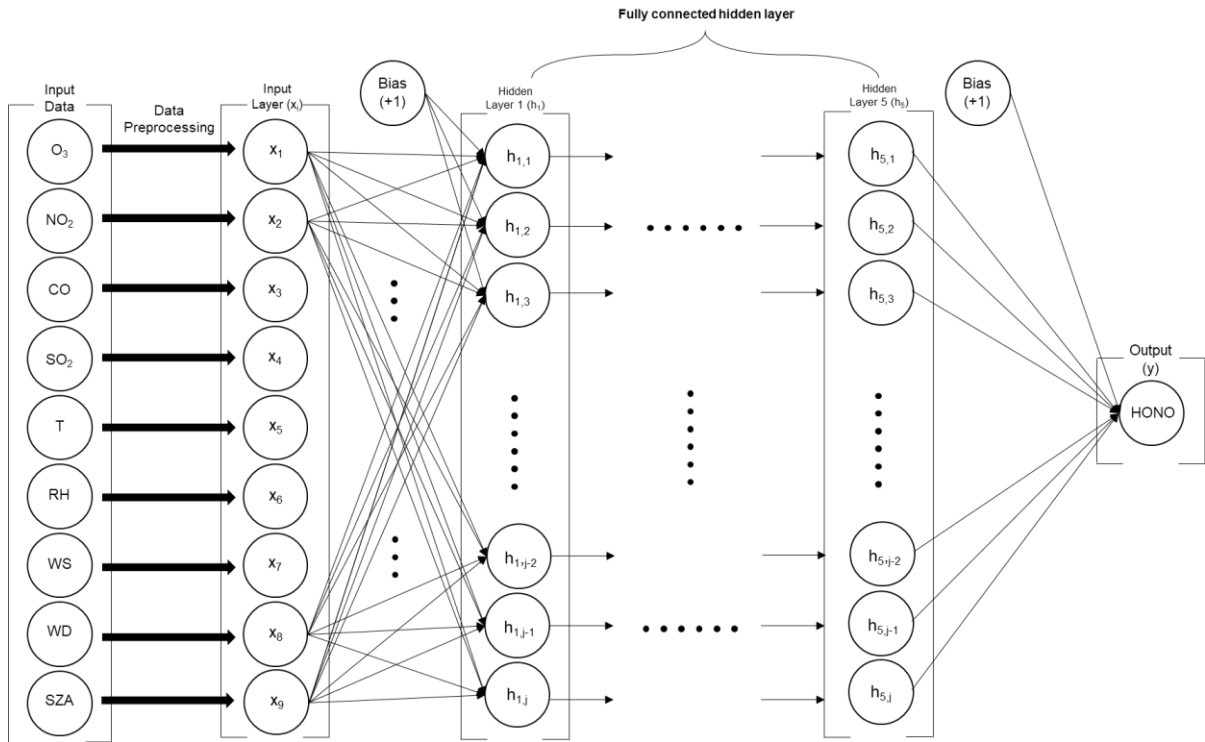
346

347 The authors declare that they have no conflict of interest.

348



352 **Figure 1.** The main processes for configuring RNDv1.0 (*: calculated values)

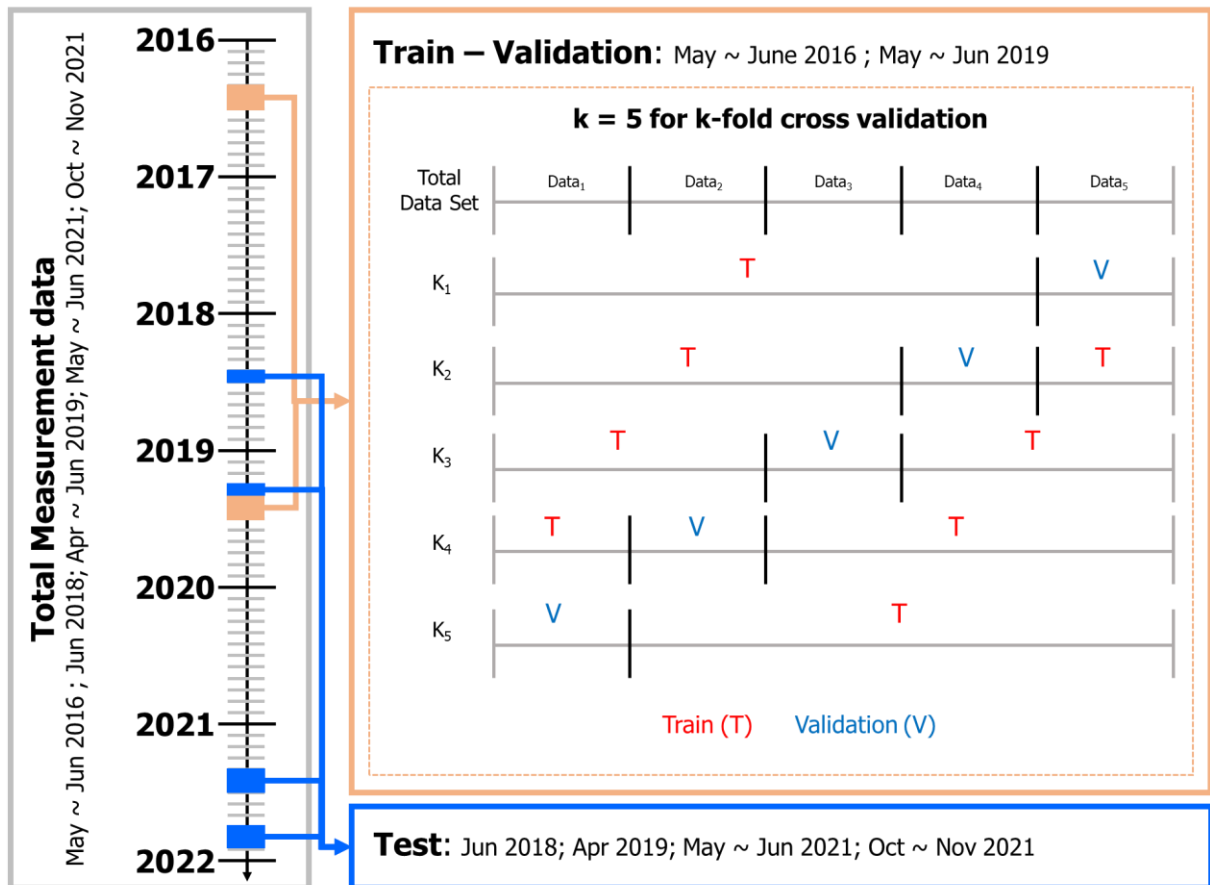


353

354 **Figure 2.** Structure of the deep neural network built for RND v1.0.

355

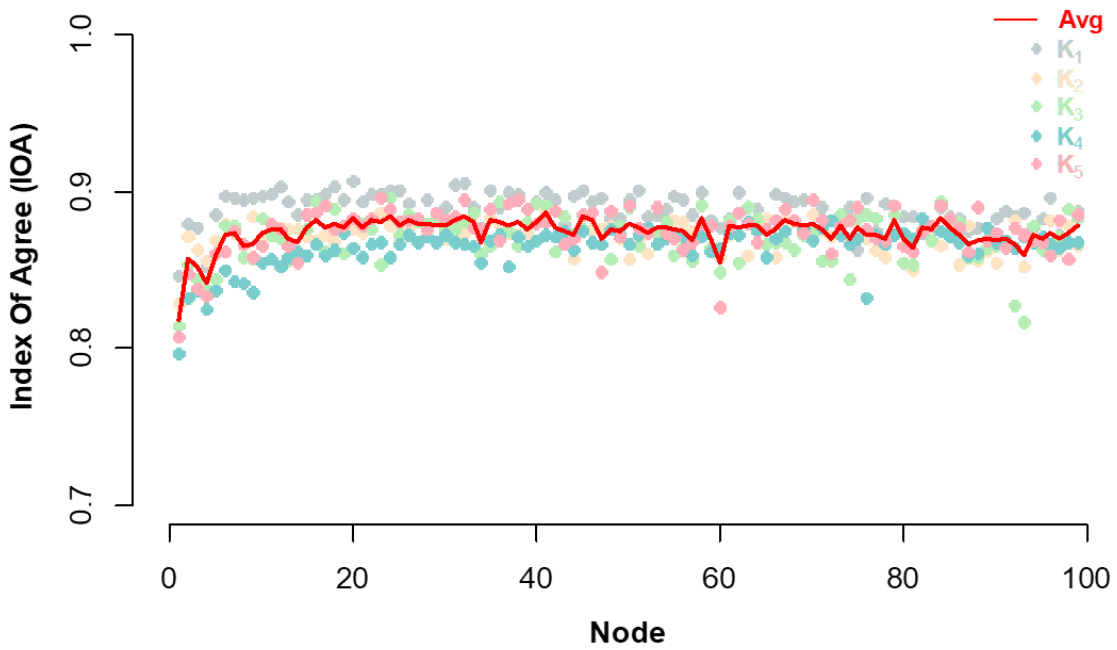
356



357

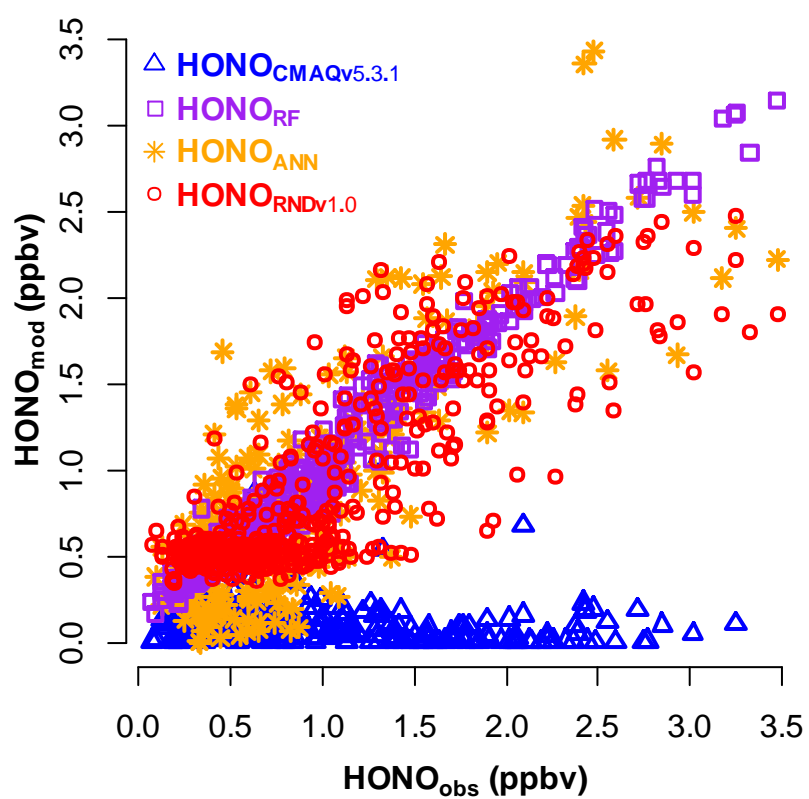
358 **Figure 3.** Training, validation, and test design to build RNDv1.0 using the measurement data.
 359 The k-fold cross validation was performed using randomly divided five subsets of the training
 360 data set.

361



362

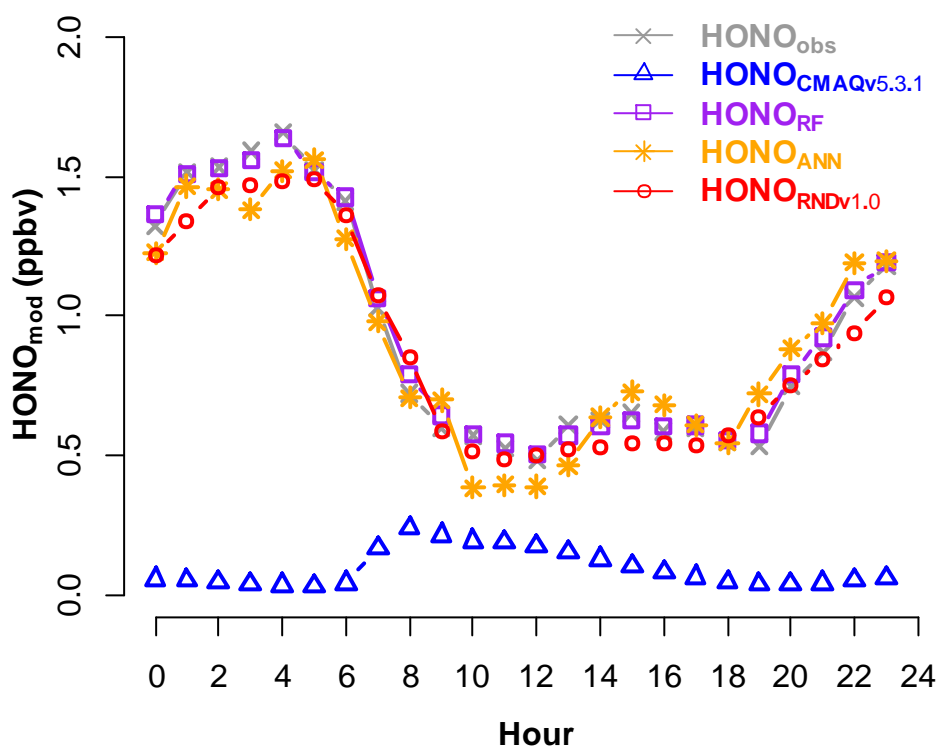
363 **Figure 4.** Index of Agreement (IOA) for k-fold cross validation. Solid circle and red line
 364 represent IOA for each validation ($k = 5$) and the average of five validation sets at each node
 365 number.



366

367 **Figure 5.** Comparison between the measured HONO (HONO_{obs}) and calculated HONO
 368 (HONO_{mod}) using CMAQv5.3.1 (blue triangle), RF (purple square), ANN (orange star), and
 369 RNDv1.0 (red circle) during the KORUS-AQ campaign (May–June 2016).

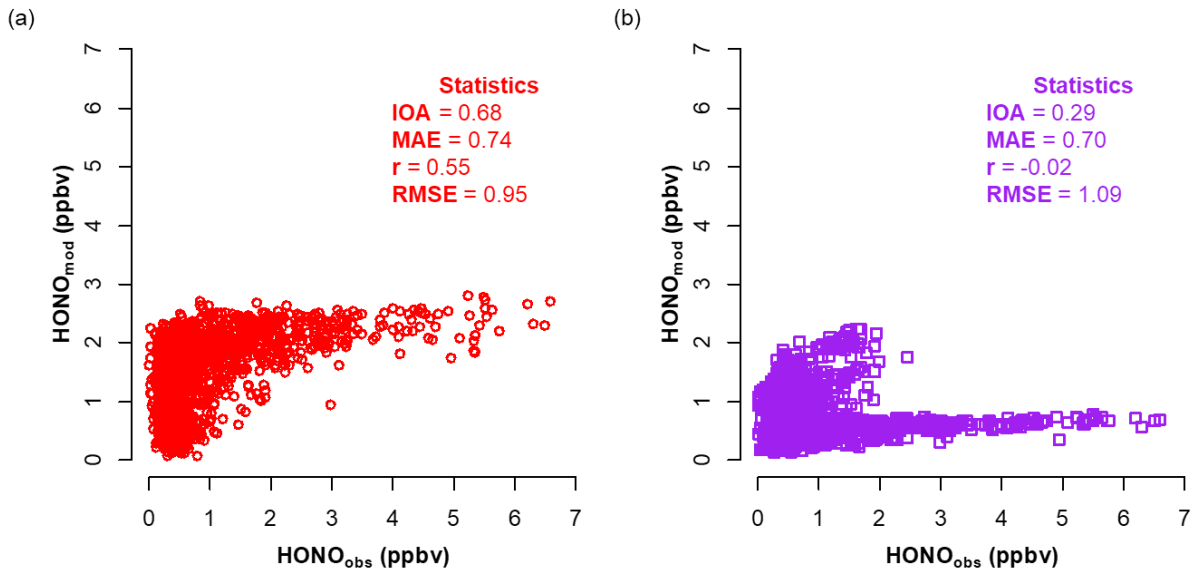
370



371

372 **Figure 6.** Average diurnal variation of the measured HONO (HONO_{obs}) and calculated
 373 HONO (HONO_{mod}) using CMAQv5.3.1 (blue triangle), RF (purple square), ANN (orange
 374 star), and RNDv1.0 (red circle) during the KORUS-AQ campaign (May–June 2016).

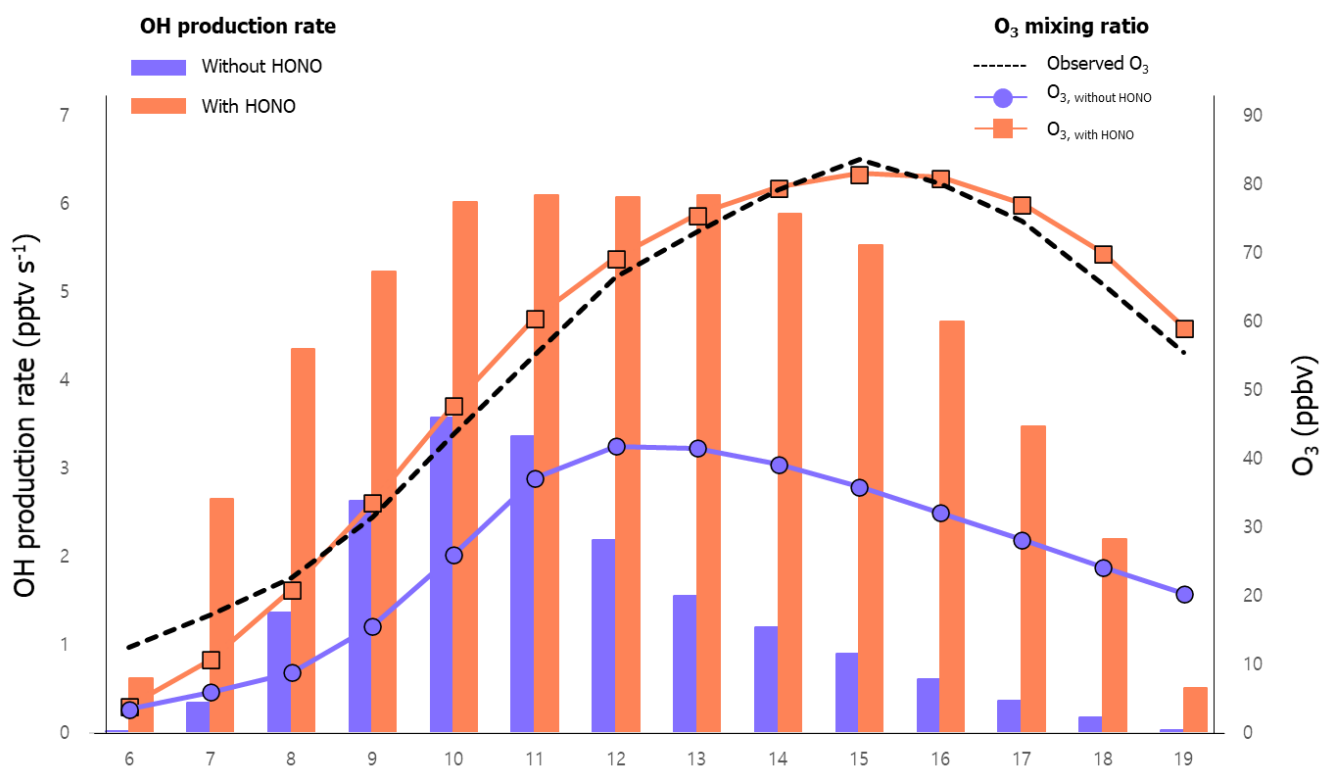
375



376

377 **Figure 7.** Relationship between measured HONO (HONO_{obs}) and modeled HONO (HONO_{mod})
378 using (a) RNDv1.0 and (b) a Random Forest model for the test dataset.

379



381

382 **Figure 8.** For June 2016, the diurnal variations of O₃ (line) and OH production rate (bar)
 383 calculated using the FOAM photochemical model with (orange) and without (blue) HONO
 384 estimated from the RNDv1.0 model. The measured and calculated O₃ values are compared.

385

386 **Table 1.** Resources for constructing the RND model.

	Version	Remark
Python	v3.8.3	
CUDA	v10.1	*If using GPU
CuDNN	v7.6.5	*If using GPU
Tensorflow	v2.3.0	<i>Python library</i>
Keras	v2.4.3	<i>Python library</i>
Pandas	v1.0.5	<i>Python library</i>
Numpy	v1.18.5	<i>Python library</i>

387 *GPU denotes graphic processing unit

388 **Table 2.** Input variables and their concentrations (10th–90th percentile of the hourly
 389 measurements), coverage, and scale factors for the RNDv1.0 model. Measurements were
 390 conducted in Seoul during May–June in 2016 and 2019.

	10 th –90 th percentile (unit)	Coverage (%)	Scale Factor1 (F ₁)*	Scale Factor 2 (F ₂)**
Input Variables				
O ₃	12.1–90.4 (ppbv)	95.5	204.738	0.842
NO ₂	11.0–48.6 (ppbv)	80.6	79.925	2.375
CO	252–743 (ppbv)	95.1	975.248	137.253
SO ₂	1.9–6.4 (ppbv)	95.6	12.479	0.958
Solar Zenith Angle	22.7–118.4 (°)	100.0	112.317	14.195
Temperature	15.9–26.7 (°C)	99.4	24.240	8.610
Relative Humidity	29.2–79.1 (%)	99.4	88.545	10.555
Wind Speed	0.2–3.7 (m/s)	99.4	7.581	0.005
Wind Direction	45.4–287.5 (°)	99.4	359.565	0.235
Output Variables				
HONO	0.3–2.0 (ppbv)	81.1 %	3.447	0.013

391 * Maximum–Minimum

392 ** Minimum value

393

394 **Table 3.** Performance of the chemical transport model (CMAQv5.3.1) and machine learning
395 (ML) models, including Random Forest (RF), Artificial Neural Network (ANN), and RNDv1.0,
396 on the measurement data from 2016 KORUS-AQ campaign, which were used for training.

	CMAQv5.3.1	RF	ANN	RNDv1.0
IOA	0.44	0.99	0.86	0.9
r	-0.07	0.99	0.81	0.84
MAE	0.82	0.1	0.38	0.27
RMSE	1.06	0.12	0.41	0.37

397

398

399 **Table 4.** Results of the bootstrap test of measurement data used to train the RF and RNDv1.0
 400 models. The greater the MAE, the greater the influence of the variable.

Variable	RF		RNDv1.0	
	MAE	Feature Importance	MAE	Feature Importance
-	0.10	-	0.28	-
O ₃	0.57	1	0.29	8
NO ₂	0.24	4	0.59	1
CO	0.19	7	0.37	5
SO ₂	0.17	8	0.34	6
Solar zenith Angle (SZA)	0.25	2	0.41	4
Temperature (T)	0.21	5	0.52	2
Relative humidity (RH)	0.25	3	0.52	2
Wind speed (WS)	0.20	6	0.34	6
Wind direction (WD)	0.13	9	0.29	8

401

402

403 **Reference**

404

- 405 Akimoto, H., Nagashima, T., Li, J., Fu, J. S., Ji, D., Tan, J., and Wang, Z.: Comparison of surface ozone simulation
406 among selected regional models in MICS-Asia III—effects of chemistry and vertical transport for the causes of
407 difference, *Atmospheric Chemistry and Physics*, 19, 603–615, 2019.
- 408 Akimoto, H., and Tanimoto, H.: Review of Comprehensive Measurements of Speciated NO_y and its Chemistry:
409 Need for Quantifying the Role of Heterogeneous Processes of HNO₃ and HONO, *Aerosol and Air Quality*
410 *Research*, 21, 200395, 2021.
- 411 Anderson, D. C., Loughner, C. P., Diskin, G., Weinheimer, A., Canty, T. P., Salawitch, R. J., Worden, H. M., Fried,
412 A., Mikoviny, T., and Wisthaler, A.: Measured and modeled CO and NO_y in DISCOVER-AQ: An evaluation of
413 emissions and chemistry over the eastern US, *Atmospheric Environment*, 96, 78–87, 2014.
- 414 Arcomano, T., Szunyogh, I., Wikner, A., Pathak, J., Hunt, B. R., and Ott, E.: A Hybrid Approach to Atmospheric
415 Modeling that Combines Machine Learning with a Physics-Based Numerical Model, *Journal of Advances in*
416 *Modeling Earth Systems*, e2021MS002712, 2021.
- 417 Armante, R., Perrin, A., Kwabia Tchana, F., and Manceron, L.: The ν₄ bands at 11 μm: linelists for the Trans- and
418 Cis-conformer forms of nitrous acid (HONO) in the 2019 version of the GEISA database, *Molecular Physics*,
419 e1951860, 2021.
- 420 Arnell, N. W., Lowe, J. A., Challinor, A. J., and Osborn, T. J.: Global and regional impacts of climate change at
421 different levels of global temperature increase, *Climatic Change*, 155, 377–391, 2019.
- 422 Baek, W.-K., and Jung, H.-S.: Performance Comparison of Oil Spill and Ship Classification from X-Band Dual-
423 and Single-Polarized SAR Image Using Support Vector Machine, Random Forest, and Deep Neural Network,
424 *Remote Sensing*, 13, 3203, 2021.
- 425 Bao, F., Cheng, Y., Kuhn, U., Li, G., Wang, W., Kratz, A. M., Weber, J., Weber, B., Pöschl, U., and Su, H.: Key
426 Role of Equilibrium HONO Concentration over Soil in Quantifying Soil–Atmosphere HONO Fluxes,
427 *Environmental science & technology*, 2022.
- 428 Bengio, Y., and Grandvalet, Y.: No unbiased estimator of the variance of K-fold cross-validation, Citeseer, 2003.
- 429 Bloss, W. J., Kramer, L., Crilley, L. R., Vu, T., Harrison, R. M., Shi, Z., Lee, J. D., Squires, F. A., Whalley, L. K.,
430 and Slater, E.: Insights into air pollution chemistry and sulphate formation from nitrous acid (HONO)
431 measurements during haze events in Beijing, *Faraday Discussions*, 226, 223–238, 2021.
- 432 Brown, S. S., An, H., Lee, M., Park, J.-H., Lee, S.-D., Fibiger, D. L., McDuffie, E. E., Dubé, W. P., Wagner, N. L.,
433 and Min, K.-E.: Cavity enhanced spectroscopy for measurement of nitrogen oxides in the Anthropocene: results
434 from the Seoul tower during MAPS 2015, *Faraday discussions*, 200, 529–557, 2017.
- 435 Canty, T., Hembeck, L., Vinciguerra, T., Anderson, D., Goldberg, D., Carpenter, S., Allen, D., Loughner, C.,
436 Salawitch, R., and Dickerson, R.: Ozone and NO_x chemistry in the eastern US: evaluation of CMAQ/CB05 with
437 satellite (OMI) data, *Atmospheric Chemistry and Physics*, 15, 10965–10982, 2015.
- 438 Chen, G., Li, S., Knibbs, L. D., Hamm, N. A., Cao, W., Li, T., Guo, J., Ren, H., Abramson, M. J., and Guo, Y.: A
439 machine learning method to estimate PM_{2.5} concentrations across China with remote sensing, meteorological and
440 land use information, *Science of the Total Environment*, 636, 52–60, 2018a.
- 441 Chen, Y., Wolke, R., Ran, L., Birmili, W., Spindler, G., Schröder, W., Su, H., Cheng, Y., Tegen, I., and Wiedensohler,
442 A.: A parameterization of the heterogeneous hydrolysis of N₂O₅ for mass-based aerosol models: improvement of
443 particulate nitrate prediction, *Atmos. Chem. Phys.*, 18, 673–689, 2018b.
- 444 Cheng, P., Pour-Biazar, A., White, A. T., and McNider, R. T.: Improvement of summertime surface ozone
445 prediction by assimilating Geostationary Operational Environmental Satellite cloud observations, *Atmospheric*
446 *Environment*, 268, 118751, 2022.
- 447 Clarisse, L., R'Honi, Y., Coheur, P. F., Hurtmans, D., and Clerbaux, C.: Thermal infrared nadir observations of 24
448 atmospheric gases, *Geophysical Research Letters*, 38, 2011.
- 449 Cui, L., and Wang, S.: Mapping the daily nitrous acid (HONO) concentrations across China during 2006–2017
450 through ensemble machine-learning algorithm, *Science of The Total Environment*, 147325, 2021.
- 451 Dang, C., Liu, Y., Yue, H., Qian, J., and Zhu, R.: Autumn crop yield prediction using data-driven approaches:-
452 support vector machines, random forest, and deep neural network methods, *Canadian Journal of Remote Sensing*,
453 47, 162–181, 2021.
- 454 Ding, B., Qian, H., and Zhou, J.: Activation functions and their characteristics in deep neural networks, 2018
455 Chinese control and decision conference (CCDC), 2018, 1836–1841.
- 456 Ge, B., Xu, X., Ma, Z., Pan, X., Wang, Z., Lin, W., Ouyang, B., Xu, D., Lee, J., and Zheng, M.: Role of Ammonia
457 on the Feedback Between AWC and Inorganic Aerosol Formation During Heavy Pollution in the North China
458 Plain, *Earth and Space Science*, 6, 1675–1693, 2019.

459 Gen, M., Liang, Z., Zhang, R., Mabato, B. R. G., and Chan, C. K.: Particulate nitrate photolysis in the atmosphere,
460 Environmental Science: Atmospheres, 2022.

461 Gil, J., Son, J., Kang, S., Park, J., Lee, M., Jeon, E., and Shim, M.: HONO measurement in Seoul during Summer
462 2018 and its Impact on Photochemistry, Journal of Korean Society for Atmospheric Environment, 36, 579-588,
463 10.5572/KOSAE.2020.36.5.579, 2020.

464 Gil, J.: RNDv1.0 and example, <https://doi.org/10.5281/zenodo.5540180>, in, Zenodo, 2021.

465 Gil, J., Kim, J., Lee, M., Lee, G., Ahn, J., Lee, D. S., Jung, J., Cho, S., Whitehill, A., Szykman, J., and Lee, J.:
466 Characteristics of HONO and its impact on O₃ formation in the Seoul Metropolitan Area during the Korea-US Air
467 Quality study, Atmospheric Environment, 2021, <https://doi.org/10.1016/j.atmosenv.2020.118182>, 2021.

468 Gil, J.: Formation pathways of HONO and its impact on O₃ and fine aerosol: based on measurement and modelling
469 study, Doctoral Thesis, 262, 2022.

470 Gu, R., Wang, W., Peng, X., Xia, M., Zhao, M., Zhang, Y., Liu, Y., Shen, H., Xue, L., and Wang, T.: Nitrous acid
471 in the polluted coastal atmosphere of the South China Sea: Ship emissions, budgets, and impacts, Science of The
472 Total Environment, 153692, 2022.

473 IPCC: Summary for policymakers. In: Climate Change 2014: Impacts, Adaption, and Vulnerability. Part A: Global
474 and Sectoral Aspects. Contribution of Working Group II to the Fifth Assessment Report of the Intergovernmental
475 Panel on Climate Change [Field, C.B., V.R. Barros, D.J. Dokken, K.J. Mach, M.D. Mastrandrea, T.E. Bilir, M.
476 Chatterjee, K.L. Ebi, Y.O. Estrada, R.C. Genova, B. Girma, E.S. Kissel, A.N. Levy, S. MacCracken, P.R.
477 Mastrandrea, and L.L. White (eds.)], Cambridge, United Kingdom and New York, NY, USA, 1-32, 2014.

478 Jia, C., Tong, S., Zhang, W., Zhang, X., Li, W., Wang, Z., Wang, L., Liu, Z., Hu, B., and Zhao, P.: Pollution
479 characteristics and potential sources of nitrous acid (HONO) in early autumn 2018 of Beijing, Science of The Total
480 Environment, 735, 139317, 2020.

481 Joutsensaari, J., Ozon, M., Nieminen, T., Mikkonen, S., Lähivaara, T., Decesari, S., Facchini, M. C., Laaksonen,
482 A., and Lehtinen, K. E.: Identification of new particle formation events with deep learning, Atmospheric Chemistry
483 and Physics, 18, 9597-9615, 2018.

484 Kang, Y., Choi, H., Im, J., Park, S., Shin, M., Song, C.-K., and Kim, S.: Estimation of surface-level NO₂ and O₃
485 concentrations using TROPOMI data and machine learning over East Asia, Environmental Pollution, 288, 117711,
486 2021.

487 Kim, H., Gil, J., Lee, M., Jung, J., Whitehill, A., Szykman, J., Lee, G., Kim, D., Cho, S., Ahn, J., Hong, J., and
488 Park, M.: Overview and characteristics of air quality in the Seoul Metropolitan Area during the KORUS-AQ
489 campaign, Elementa: Science of the Anthropocene, in review, 2020.

490 Kleffmann, J., Lörzer, J., Wiesen, P., Kern, C., Trick, S., Volkamer, R., Rodenas, M., and Wirtz, K.:
491 Intercomparison of the DOAS and LOPAP techniques for the detection of nitrous acid (HONO), Atmospheric
492 Environment, 40, 3640-3652, 2006.

493 Kleinert, F., Leufen, L. H., and Schultz, M. G.: IntelliO₃-ts v1. 0: a neural network approach to predict near-surface
494 ozone concentrations in Germany, Geoscientific Model Development, 14, 1-25, 2021.

495 Krishnamurthy, R., Newsom, R. K., Berg, L. K., Xiao, H., Ma, P.-L., and Turner, D. D.: On the estimation of
496 boundary layer heights: a machine learning approach, Atmospheric Measurement Techniques, 14, 4403-4424,
497 2021.

498 Lee, B. H., Wood, E. C., Zahniser, M. S., McManus, J. B., Nelson, D. D., Herndon, S. C., Santoni, G., Wofsy, S.
499 C., and Munger, J. W.: Simultaneous measurements of atmospheric HONO and NO₂ via absorption spectroscopy
500 using tunable mid-infrared continuous-wave quantum cascade lasers, Applied Physics B, 102, 417-423, 2011.

501 Levy, M., Zhang, R., Zheng, J., Zhang, A. L., Xu, W., Gomez-Hernandez, M., Wang, Y., and Olaguer, E.:
502 Measurements of nitrous acid (HONO) using ion drift-chemical ionization mass spectrometry during the 2009
503 SHARP field campaign, Atmospheric Environment, 94, 231-240, 2014.

504 Li, S., Song, W., Zhan, H., Zhang, Y., Zhang, X., Li, W., Tong, S., Pei, C., Wang, Y., and Chen, Y.: Contribution of
505 Vehicle Emission and NO₂ Surface Conversion to Nitrous Acid (HONO) in Urban Environments: Implications
506 from Tests in a Tunnel, Environmental Science & Technology, 55, 15616-15624, 2021a.

507 Li, Y., Wang, X., Wu, Z., Li, L., Wang, C., Li, H., Zhang, X., Zhang, Y., Li, J., and Gao, R.: Atmospheric nitrous
508 acid (HONO) in an alternate process of haze pollution and ozone pollution in urban Beijing in summertime:
509 Variations, sources and contribution to atmospheric photochemistry, Atmospheric Research, 260, 105689, 2021b.

510 Li, Z., Xie, P., Hu, R., Wang, D., Jin, H., Chen, H., Lin, C., and Liu, W.: Observations of N₂O₅ and NO₃ at a
511 suburban environment in Yangtze river delta in China: Estimating heterogeneous N₂O₅ uptake coefficients,
512 Journal of Environmental Sciences, 2020.

513 Liebmann, J., Karu, E., Sobanski, N., Schuladen, J., Ehn, M., Schallhart, S., Quéléver, L., Hellen, H., Hakola, H.,
514 and Hoffmann, T.: Direct measurement of NO₃ radical reactivity in a boreal forest, Atmospheric Chemistry and
515 Physics, 2018.

516 Liu, Y., Lu, K., Li, X., Dong, H., Tan, Z., Wang, H., Zou, Q., Wu, Y., Zeng, L., and Hu, M.: A comprehensive
517 model test of the HONO sources constrained to field measurements at rural North China Plain, *Environmental*
518 *science & technology*, 53, 3517-3525, 2019.

519 Mallet, V., and Sportisse, B.: Uncertainty in a chemistry-transport model due to physical parameterizations and
520 numerical approximations: An ensemble approach applied to ozone modeling, *Journal of Geophysical Research:*
521 *Atmospheres*, 111, 2006.

522 Meng, F., Qin, M., Fang, W., Duan, J., Tang, K., Zhang, H., Shao, D., Liao, Z., Feng, Y., and Huang, Y.:
523 Measurement of HONO flux using the aerodynamic gradient method over an agricultural field in the Huaihe River
524 Basin, China, *Journal of Environmental Sciences*, 2022.

525 Monks, P. S., Archibald, A., Colette, A., Cooper, O., Coyle, M., Derwent, R., Fowler, D., Granier, C., Law, K. S.,
526 and Mills, G.: Tropospheric ozone and its precursors from the urban to the global scale from air quality to short-
527 lived climate forcer, *Atmospheric Chemistry and Physics*, 15, 8889-8973, 2015.

528 Myhre, G., Aas, W., Cherian, R., Collins, W., Faluvegi, G., Flanner, M., Forster, P., Hodnebrog, Ø., Klimont, Z.,
529 and Lund, M. T.: Multi-model simulations of aerosol and ozone radiative forcing due to anthropogenic emission
530 changes during the period 1990–2015, *Atmospheric Chemistry and Physics*, 17, 2709-2720, 2017.

531 Pinto, J., Dibb, J., Lee, B., Rappenglück, B., Wood, E., Levy, M., Zhang, R. Y., Lefter, B., Ren, X. R., and Stutz,
532 J.: Intercomparison of field measurements of nitrous acid (HONO) during the SHARP campaign, *Journal of*
533 *Geophysical Research: Atmospheres*, 119, 5583-5601, 2014.

534 Reichstein, M., Camps-Valls, G., Stevens, B., Jung, M., Denzler, J., and Carvalhais, N.: Deep learning and process
535 understanding for data-driven Earth system science, *Nature*, 566, 195-204, 2019.

536 Roberts, J. M., Veres, P., Warneke, C., Neuman, J., Washenfelder, R., Brown, S., Baasandorj, M., Burkholder, J.,
537 Burling, I., and Johnson, T. J.: Measurement of HONO, HNCO, and other inorganic acids by negative-ion proton-
538 transfer chemical-ionization mass spectrometry (NI-PT-CIMS): Application to biomass burning emissions,
539 *Atmospheric Measurement Techniques*, 3, 981, 2010.

540 Schultz, M., Betancourt, C., Gong, B., Kleinert, F., Langguth, M., Leufen, L., Mozaffari, A., and Stadtler, S.: Can
541 deep learning beat numerical weather prediction?, *Philosophical Transactions of the Royal Society A*, 379,
542 20200097, 2021.

543 Shahriar, S. A., Kayes, I., Hasan, K., Salam, M. A., and Chowdhury, S.: Applicability of machine learning in
544 modeling of atmospheric particle pollution in Bangladesh, *Air Quality, Atmosphere & Health*, 13, 1247-1256, 2020.

545 Shareef, M. M., Husain, T., and Alharbi, B.: Studying the Effect of Different Gas-Phase Chemical Kinetic
546 Mechanisms on the Formation of Oxidants, Nitrogen Compounds and Ozone in Arid Regions, *Journal of*
547 *Environmental Protection*, 10, 1006-1031, 2019.

548 Shindell, D. T., Lamarque, J.-F., Schulz, M., Flanner, M., Jiao, C., Chin, M., Young, P., Lee, Y. H., Rotstayn, L.,
549 and Mahowald, N.: Radiative forcing in the ACCMIP historical and future climate simulations, *Atmospheric*
550 *Chemistry and Physics*, 13, 2939-2974, 2013.

551 Stadtler, S., Simpson, D., Schröder, S., Taraborrelli, D., Bott, A., and Schultz, M.: Ozone impacts of gas-aerosol
552 uptake in global chemistry transport models, *Atmospheric chemistry and physics*, 18, 3147-3171, 2018.

553 Stevenson, D., Young, P., Naik, V., Lamarque, J.-F., Shindell, D. T., Voulgarakis, A., Skeie, R. B., Dalsoren, S. B.,
554 Myhre, G., and Berntsen, T. K.: Tropospheric ozone changes, radiative forcing and attribution to emissions in the
555 Atmospheric Chemistry and Climate Model Intercomparison Project (ACCMIP), *Atmospheric Chemistry and*
556 *Physics*, 13, 3063-3085, 2013.

557 Sumathi, S., and Pugalendhi, G. K.: Cognition based spam mail text analysis using combined approach of deep
558 neural network classifier and random forest, *Journal of Ambient Intelligence and Humanized Computing*, 12,
559 5721-5731, 2021.

560 Sun, Y., Wang, L., Wang, Y., Quan, L., and Zirui, L.: In situ measurements of SO₂, NO_x, NO_y, and O₃ in Beijing,
561 China during August 2008, *Science of the Total Environment*, 409, 933-940, 2011.

562 Theys, N., Volkamer, R., Müller, J.-F., Zarzana, K. J., Kille, N., Clarisse, L., De Smedt, I., Lerot, C., Finkenzeller,
563 H., and Hendrick, F.: Global nitrous acid emissions and levels of regional oxidants enhanced by wildfires, *Nature*
564 *geoscience*, 13, 681-686, 2020.

565 Tie, X., Geng, F., Guenther, A., Cao, J., Greenberg, J., Zhang, R., Apel, E., Li, G., Weinheimer, A., and Chen, J.:
566 Megacity impacts on regional ozone formation: observations and WRF-Chem modeling for the MIRAGE-
567 Shanghai field campaign, *Atmospheric Chemistry and Physics*, 13, 5655-5669, 2013.

568 VandenBoer, T., Markovic, M., Sanders, J., Ren, X., Pusede, S., Browne, E., Cohen, R., Zhang, L., Thomas, J.,
569 and Brune, W. H.: Evidence for a nitrous acid (HONO) reservoir at the ground surface in Bakersfield, CA, during
570 CalNex 2010, *Journal of Geophysical Research: Atmospheres*, 119, 9093-9106, 2014.

571 Varotsos, K., Giannakopoulos, C., and Tombrou, M.: Assessment of the Impacts of climate change on european
572 ozone levels, *Water, Air, & Soil Pollution*, 224, 1-13, 2013.

573 Wang, H., Chen, X., Lu, K., Hu, R., Li, Z., Wang, H., Ma, X., Yang, X., Chen, S., and Dong, H.: NO₃ and N₂O₅
574 chemistry at a suburban site during the EXPLORE-YRD campaign in 2018, *Atmospheric Environment*, 224,
575 117180, 2020.

576 Wang, T., Qin, Z., and Zhu, M.: An ELU network with total variation for image denoising, *International Conference*
577 *on Neural Information Processing*, 2017a, 227-237.

578 Wang, X., Wang, H., Xue, L., Wang, T., Wang, L., Gu, R., Wang, W., Tham, Y. J., Wang, Z., and Yang, L.:
579 Observations of N₂O₅ and ClNO₂ at a polluted urban surface site in North China: High N₂O₅ uptake coefficients
580 and low ClNO₂ product yields, *Atmospheric environment*, 156, 125-134, 2017b.

581 Wolfe, G. M., Marvin, M. R., Roberts, S. J., Travis, K. R., and Liao, J.: The framework for 0-D atmospheric
582 modeling (F0AM) v3. 1, *Geoscientific Model Development*, 9, 3309, 2016.

583 Xu, Z., Liu, Y., Nie, W., Sun, P., Chi, X., and Ding, A.: Evaluating the measurement interference of wet rotating-
584 denuder-ion chromatography in measuring atmospheric HONO in a highly polluted area, *Atmospheric*
585 *Measurement Techniques*, 12, 6737-6748, 2019.

586 Xue, C., Ye, C., Ma, Z., Liu, P., Zhang, Y., Zhang, C., Tang, K., Zhang, W., Zhao, X., and Wang, Y.: Development
587 of stripping coil-ion chromatograph method and intercomparison with CEAS and LOPAP to measure atmospheric
588 HONO, *Science of The Total Environment*, 646, 187-195, 2019.

589 Ye, C., Zhou, X., Pu, D., Stutz, J., Festa, J., Spolaor, M., Tsai, C., Cantrell, C., Mauldin, R. L., and Campos, T.:
590 Rapid cycling of reactive nitrogen in the marine boundary layer, *Nature*, 532, 489-491, 2016.

591